remote sensing

MDPI

Article

Detection of Oil Spills in the Northern South China Sea Using Landsat-8 OLI

Xiaorun Hong [1,†], Lusheng Chen [2,†], Shaojie Sun [2,3,4,5,*], Zhen Sun [6], Ying Chen [2], Qiang Mei [7] and Zhichao Chen [2]

[1] School of Geography and Planning, Sun Yat-sen University, Guangzhou 510006, China
[2] School of Marine Sciences, Sun Yat-sen University, Zhuhai 519082, China
[3] Southern Marine Science and Engineering Guangdong Laboratory (Zhuhai), Zhuhai 519000, China
[4] Guangdong Provincial Key Laboratory of Marine Resources and Coastal Engineering, Guangzhou 510275, China
[5] Pearl River Estuary Marine Ecosystem Research Station, Ministry of Education, Zhuhai 519000, China
[6] School of Marine Engineering and Technology, Sun Yat-sen University, Zhuhai 519082, China
[7] Navigation College, Jimei University, Xiamen 361021, China
* Correspondence: sunshj7@mail.sysu.edu.cn; Tel.: +86-186-6697-2696
† These authors contributed equally to this work.

Abstract: Petroleum extraction, transportation, and consumption in the marine environment contribute to a large portion of anthropogenic oil spills into the ocean. While previous research focuses more on large oil spill accidents from oil tankers or offshore oil platforms, there are few systematic records on occasional regional oil spills. In this study, optical imagery from Landsat-8 OLI was used to detect oil slicks on the ocean surface through spatial analysis and spectral diagnosis in the northern South China Sea (NSCS). The source of the slicks was identified through datasets from traffic density and platform locations. A total of 632 oil slicks were detected in the NSCS from 2015 to 2019, where 57 were from platforms sources, and 490 were from ships. The average area of the detected slicks was 4.8 km^2, and half of the slicks had areas <1.7 km^2. Major oil spill hot spots included coastal Guangdong (ship origins), southeast and northeast Dongsha Island (ship origins), middle of south Beibu Gulf (ship and platform origins), and southeast Pearl River Estuary (platform origins). Through this study, we demonstrate the capability of medium-resolution optical imagery in monitoring regional oil spills. Such results and methods may help in near real-time oil spill monitoring and further environmental assessments.

Keywords: oil spills; remote sensing; spill origin; northern South China Sea

check for updates

Citation: Hong, X.; Chen, L.; Sun, S.; Sun, Z.; Chen, Y.; Mei, Q.; Chen, Z. Detection of Oil Spills in the Northern South China Sea Using Landsat-8 OLI. *Remote Sens.* **2022**, *14*, 3966. https://doi.org/10.3390/rs14163966

Academic Editors: Zhixiang Fang, Xiaofeng Li, Quanyi Huang, Jaroslaw Tęgowski, Magaly Koch and Yukiharu Hisaki

Received: 12 July 2022
Accepted: 11 August 2022
Published: 15 August 2022

1. Introduction

Oil spills in the ocean may have an adverse impact on the marine environment. The 2010 Deepwater Horizon oil spill leaked more than 3 million barrels of oil into the Gulf of Mexico (GoM) and was demonstrated to have greatly affected the marine habitat and the local environment [1]. The Iranian oil tanker SANCHI, carrying 1 million barrels of condensate oil, collided with a grain freighter in 2018, causing fires and sinking and released carried oil into the East China Sea [2]. In 2020, the Japanese bulk carrier Wakashio hit Pt d'Esny Coral Reef in Mauritius, leaking oil into a lagoon composed of a variety of habitats including beaches, mangroves, swamps, seagrass beds, and coral reefs [3].

Such large oil spill accidents attract lots of public attention; however, small-sized oil spills happen more frequently and may leak more volume than large spill accidents. According to statistics from ITOPF [4], over 80% of oil spill incidents recorded were small spills (<7 tons) since 1970. Moreover, accident spills and operational discharges from non-tanker vessels alone contribute to >20% of the total spilled volume annually, though they usually would not lead to large spill accidents [5]. Sources of oil in the marine environment can be categorized into four types: oil extraction, transportation (including oil tankers, pipelines, etc.), consumption (including land runoff, non-tank vessel spill, and operational discharge), and natural seeps [5,6], which correspond to 3%, 12%, 38%, and 47% of total spilled volume worldwide according to statistics from 1990 to 1999 [5]. A recent study has found that anthropogenic oil spills are one order of magnitude larger than spills from natural seeps globally (94% vs. 6%) [7], according to data from 2014 to 2019.

Monitoring all the oil spills in the ocean is not trivial [8,9]. The U.S. National Response Center theoretically records leaked oil that can cause surface discoloration or deposited sludge/emulsion below the ocean surface in U.S. waters [10]. However, such records are reported mainly by responsible parties (polluters) or third parties (passers-by), and their reports on spill location and magnitude are not validated independently [11]. Some researchers statistically report regional oil spills in a certain period [12,13]. Though statistical data show oil spill area and frequency, we know little about spatial distributions of the oil spills. Moreover, such records are usually not up-to-date. In addition, since such records usually focus on large spill accidents, data of those small-sized spills are regularly blank.

With characteristics of wide coverage, and rapid, continuous, and periodic imaging, remote sensing nowadays plays an important role in oil spill detection on the sea surface [14–16]. Many remote sensing techniques serve this purpose, including Synthetic Aperture Radar (SAR), optical remote sensing, and thermal remote sensing [17–19]. The Sentinel-1 SAR and ENVISAT ASAR were used to interpret oil spills in the western Java Sea [20]. Oil spills in the Eastern Arabian Sea were extracted by Sentinel-1 SAR to study the year-to-year variability of oil spills [21]. Both the above studies were conducted through visual inspection and manual delineation/clustering of oil pixels based on the spatial contrast and shape of the oil spills. During the 2010 Deepwater Horizon oil spill, the released oil was effectively mapped by SAR through a Textural Classifier Neural Network Algorithm [22], with the resulting cumulative oil coverage in the GoM comparable to results from the optical MODIS and MERIS interpretation (within 16%) [23].

Oil spills can also be differentiated by optical remote sensing through spatial and spectral analyses. The optical MODIS images are used to detect natural oil slicks in the northwestern GoM through spatial contrast under sun glint, with the comparable slick area in same-day SAR detection [24]. Oil slick spatial contrasts and spectral characteristics have been interpreted in Landsat (TM, ETM+, OLI) and Sentinel-2 MSI images to manually delineate chronic spills from an abandoned platform in the GoM with areal relative error ~50% from same-day detection of SAR and other optical sensors [25]. In this study, the recurring, long time series Landsat OLI imagery was used to detect and statistically analyze oil spills (small- and large-sized) in the northern South China Sea (NSCS) from 2015 to 2019. The study has two objectives. First, we hope to demonstrate remote sensing capabilities in oil spill monitoring on a regional scale. Second, by accessing databases from oil production platforms and marine traffic, the sources of the detected oil slicks can be determined.

2. Data

2.1. Study Area

Figure 1 shows the study area of this research in the NSCS (~105°–121°E, ~16°–25°N). The South China Sea (SCS) is a semi-enclosed basin, located between the Pacific Ocean and the Indian Ocean, and is one of the world's four major oil and gas accumulation centers, with proven oil reserves of 6.4 billion tons and natural gas reserves of 980 billion m^3 [26]. Main oil and gas reserves of Pearl River Mouth Basin, Beibu Gulf Basin, Yinggehai Basin, and southeast Qiong basin are included in the study area [26]. Moreover, the SCS is an important hub of international strategic material transportation for East Asian countries, with particularly high ship traffic in the NSCS. According to Chang and Yang [27], oil transported through the SCS accounts for half of the world's total oil transportation volume each year.

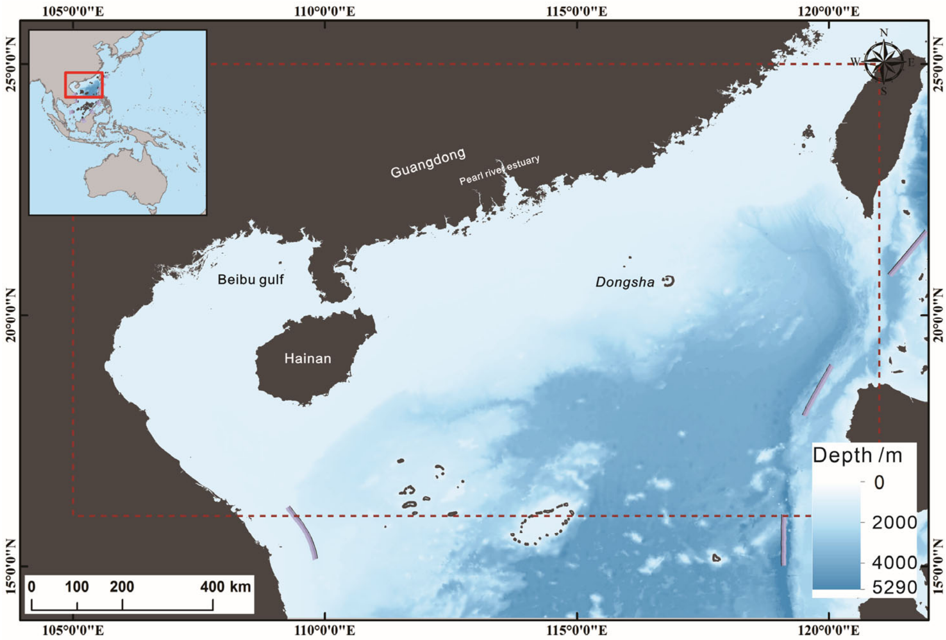

Figure 1. The study area (longitude ~105°–121°E, latitude ~16°–25°N).

2.2. Satellite Datasets

Satellite images used in this study include the Landsat-8 OLI from 2015 to 2019 and selected PlanetScope imagery in 2018 and 2019. Landsat-8 OLI images were downloaded from the United States Geological Survey (USGS), with a spatial resolution of 30 m for multispectral bands. OLI images were then processed to Rayleigh-corrected reflectance (Rrc, dimensionless) using the ACOLITE (version 20211124.0, https://github.com/acolite, accessed on 18 January 2022). ACOLITE is a generic processor developed at the Royal Belgian Institute of Natural Sciences for atmospheric correction and processing for aquatic applications of medium to high resolution optical imagery, including Landsat, Sentinel-2, PlanetScope, etc. [28]. PlanetScope 3-band Top of Atmospheric reflectance data (~3 m spatial resolution) were obtained from Planet labs [29]. It is noted that the standard PlanetScope data are usually not provided for regions >15 km from shoreline except for the 3-band data in red-green-blue channels. Same day PlanetScope images at the determined slick locations by OLI were downloaded from March to October 2018. The 3-band RGB images were then used to identify oil presence and delineate slick distribution. Table 1 listed the specifications of the satellite imagery used in this study.

Table 1. Specifications of the satellite image used in this study.

Sensor	Resolution	Revisit Time	Wavelength (nm)	Bands	Running Time	Source
OLI	30 m	16 days	430–2290	8	2013–now	USGS
PlanetScope	~3 m	1–2 days	455–875	3–8	2014–now	Planet labs

Of the many remote sensing techniques used for oil spill detection, SAR and optical remote sensing are most frequently used [14,19]. The optical OLI imagery was used in this study for oil detection because OLI has regular coverage both for near shoreline and offshore waters, and its dataset was publicly available over the study period. The PlanetScope imagery in this study was used for cross-checking purposes over the selected period.

2.3. Oil Slick Detection by OLI

In optical imagery, spatial contrasts between oil and clear water pixels are mainly caused by two factors: oil has its unique optical properties, which feature strong absorption in the blue and exponentially decay toward longer wavelengths; the coverage of an oil slick can dampen sea surface capillary and short gravity waves, enhancing the contrast between oil and water under sun glint [30]. The latter also applies for oil slick detection by SAR [14]. Because of the high absorption, thick crude oil would usually display lower than background water reflectance in the visible wavelengths, with the largest contrast in the blue–green bands depending on background water optical properties [30]. The oil–water mixing in the oil emulsions enables high scattering and thus elevated reflectance in the red, Near InfraRed (NIR), and ShortWave InfraRed (SWIR) bands. Under sun glint, oil would show either positive or negative contrast with nearby uncontaminated water, which demonstrates higher or lower than water reflectance over the spectral bands [30,31]. Moreover, oil slicks usually have elongated shapes and exhibit sharp edges in a sun glint image because of oil's dampening effect [32].

The above principles were used to discriminate oil from uncontaminated seawater in this study. Firstly, enhanced RGB true color images were visually inspected to check spatial anomalies; the anomalies were then diagnosed spatially and spectrally to eliminate oil look-alikes. After spatial/spectral diagnoses, the identified oil slicks were finally delineated in software ArcMap (version 10.6, Environment System Research Institute, Redlands, CA, USA). The flowchart in Figure 2 summarizes the oil slick extraction procedures.

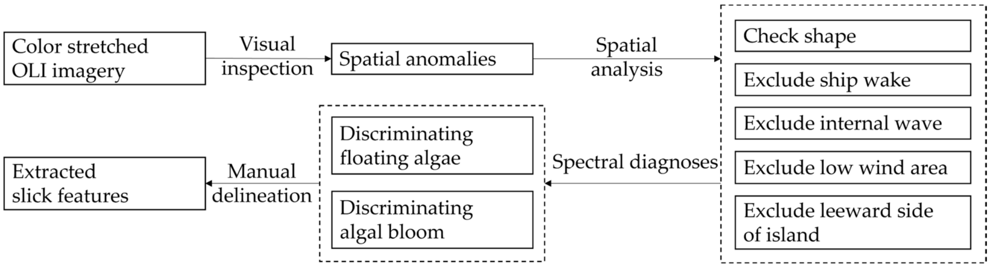

Figure 2. Flowchart of oil slick feature extraction procedures.

As mentioned, oil displays either positive or negative contrast or partly positive and partly negative contrast with water [24,32]. In this study, the bright slick or slick part (positive oil–water contrast) of the anomaly feature was spectrally diagnosed. The corresponding dark slick or slick part under sun glint (negative oil–water contrast), mostly resampled water spectra but with a lower reflectance, was usually diagnosed through the feature's morphology (e.g., typical shapes from ship wake, internal waves, etc.). Figure 3a shows Rrc spectra from oil slicks of the dark and bright parts and seawater under sun glint. Generally, bright slicks' reflectance was higher than water's, while dark slick reflectance was lower than water's (Figure 3b), which is mainly attributed to the sun glint effect caused by oil's wave dampening.

Oil look-alikes were ruled out through a combination of spectral diagnosis and shape analysis. Such oil-resembled features in optical imagery include floating algae, ship wake, internal waves, etc. Ship wake is a kind of trace left on the water surface by a moving ship, which is usually presented by one or two straight lines and could extend over several kilometers. Once formed, the ship wake would last from minutes to several hours, with the shape of the slicks changing with time because of the current movement. Ship wakes generally appear as a V-shape with a dark region between two wake arms in remote sensing imagery [33,34]. Figure 4 shows a transect of the ship wake perpendicular to the ship's driving direction, presenting two bright lines at the edge of the V-shape and a dark region within the V-shape following the ship. As shown in Figure 4, the reflectance elevation at the edge and depression between the two lines were clearly demonstrated from the reflectance of the 561-nm and 865-nm bands. Similar brightness reversal happens in images with internal waves. Figure 5 shows internal waves that happened 120 km west of the Dongsha Island in May 2016, which featured alternating bands of light and dark strips in the OLI image. Such a reflectance anomaly was caused by variations of roughness on the surface (Figure 5b), which can be effectively differentiated from oil slicks in OLI imagery.

In addition to ship wakes and internal waves, the leeward side of an island and low wind areas can also be differentiated because of direct attachment to islands and extensive dark areas with scattered dark patches at the borders, respectively.

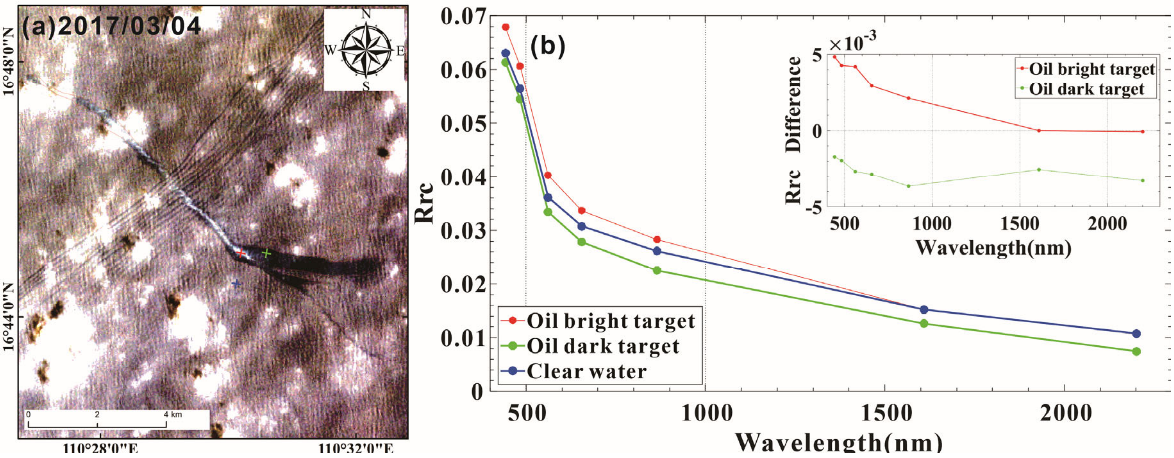

Figure 3. (**a**) Outlined oil slicks in the NSCS: (**b**) Rrc reflectance spectra from the marked points in panel a. The inset shows the Rrc difference (oil–water) between oil and clear water.

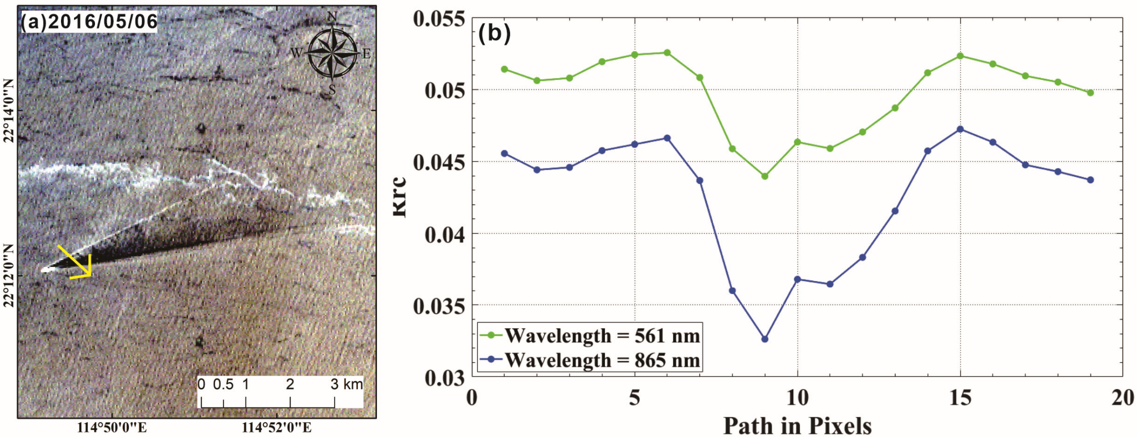

Figure 4. (**a**) Ship wakes on the ocean surface; (**b**) Rrc spectra at 561-nm and 865-nm bands along the transect marked in panel a (yellow arrow).

Floating algae of various forms could resample oil slicks in optical imagery [35]. tides are widely distributed along the coast of Guangdong and Guangxi Province, China, with red tide blooms happening mostly from March to June each year [36,37]. Figure 6 shows typical red tide events that usually happen near the Guangdong coast, presenting dark patches in the RGB image. The Rrc spectra show decreased reflectance in the blue to green bands (Figure 6b). The dark color and the decreased reflectance in blue–green bands resemble thick crude oil in optical imagery [30]. However, such surface algal blooms are usually sparsely distributed, while oil slicks typically demonstrate sharp edges (drastic reflectance change across the edge). Considering the distribution pattern and the bloom season, such a red tide could still be discriminated from those small-sized spills from ships or platforms. Figure 7 demonstrates the appearance of blooms from Red *Noctiluca Scintillans*, which feature high absorption in the blue bands and elevated reflectance in the near-infrared bands [38]. With these above characteristics, the spatial contrast caused by algal blooms or floating algae can be excluded through spatial and spectral analysis.

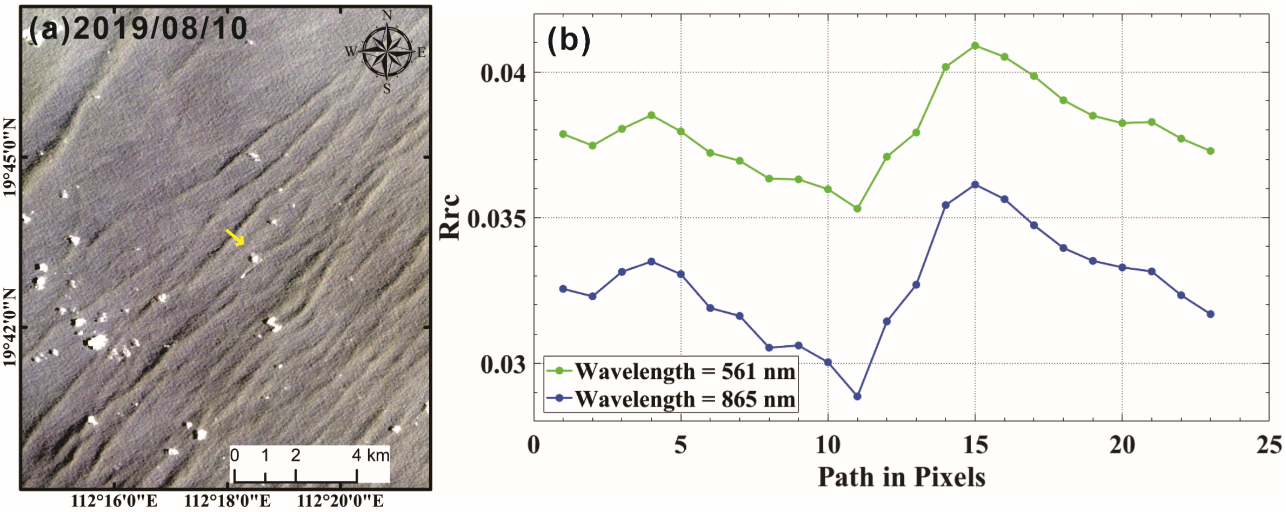

Figure 5. (**a**) Internal wave presented as alternating bands of light and dark strips; (**b**) Rrc reflectance at 561-nm and 865-nm bands along the transect marked in panel a (yellow arrow).

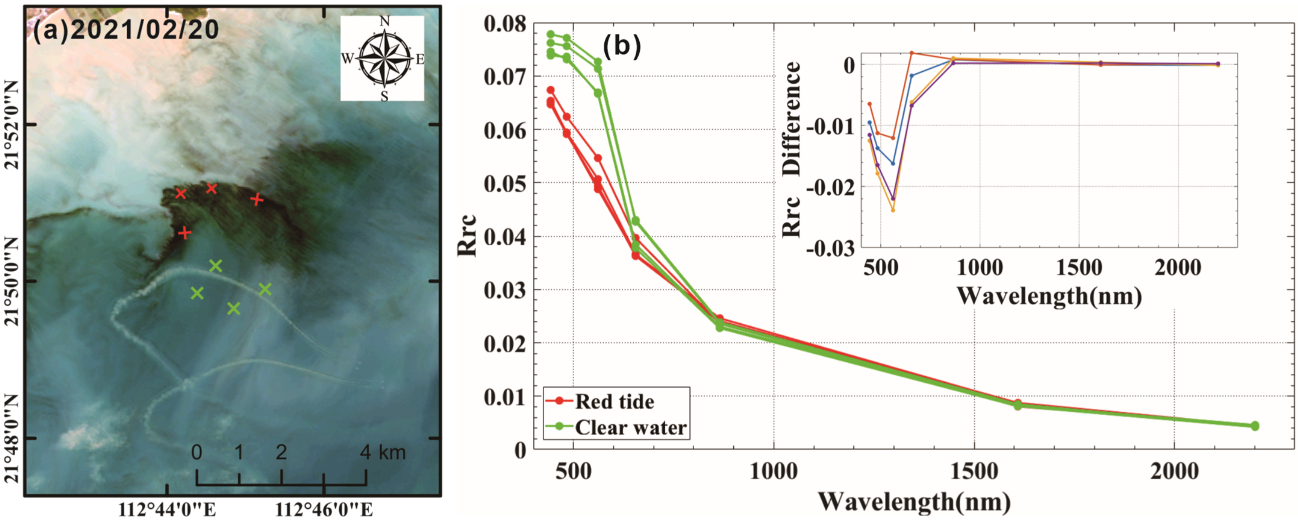

Figure 6. (**a**) Typical red tide blooms near Yangjiang; (**b**) spectral curves of selected red tide blooms and nearby water pixels marked as red and green crosses in panel a, respectively; The inset shows the Rrc difference between red tide and nearby water.

Slick features partially blocked by small cloud (scattered cloud) or other objects would be connected through visual interpretation in the delineation process (e.g., in Figure 2). If the slick feature was under complete cloud cover, it would not be detected through the OLI image. Or, if a large portion of the slicks was under cloud cover, such slicks would not be delineated for areal analysis. To be conservative, all delineated slicks with an area <0.2 km^2 (corresponding to slicks ~1 km in length and ~200 m in width, not including the detached ones from a major slick, where they were defined as one slick in this study) were excluded from the dataset.

2.4. Offshore Platform Database and Traffic Densities

An offshore platform database in the study area was overlaid to determine if the detected oil slicks originated from oil and gas platforms. The offshore platform database was retrieved through a time series remote sensing approach [39], which includes information on platform location, its status (physically removed or not), the installation date, and the removal date (if removed) of the platforms. In this study, if a platform was directly associated with one end of the oil slick, then the detected slick was determined to be originating from the corresponding platform.

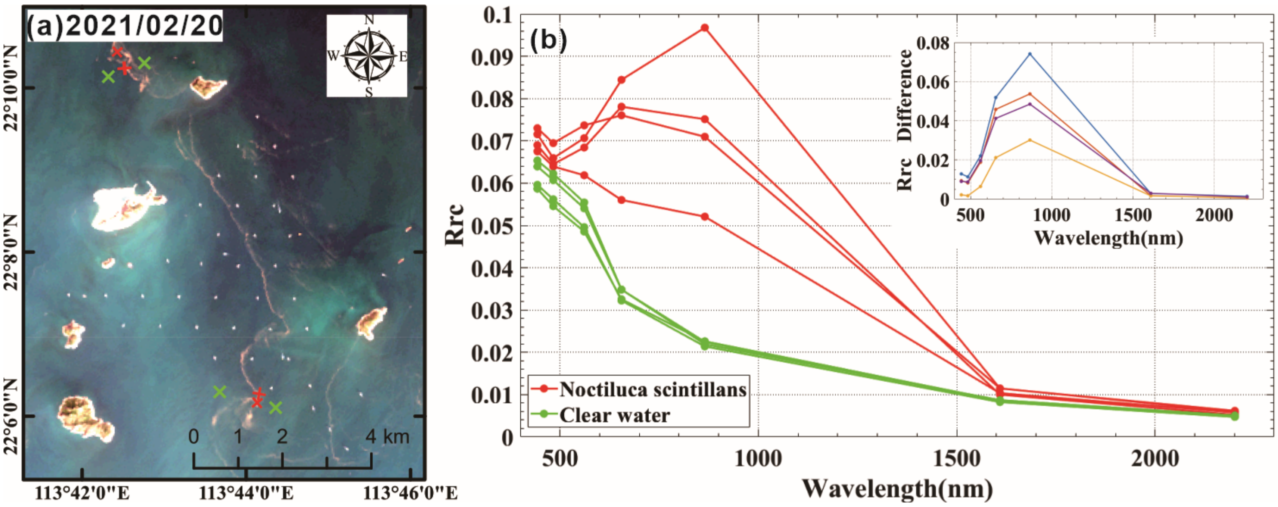

Figure 7. (**a**) Red *Noctiluca Scintillans* bloom in the Pearl River Estuary; (**b**) spectral curves of selected Red *Noctiluca Scintillans* and nearby water pixels marked as red and green crosses in panel a, respectively. The inset shows the Rrc difference between Red *Noctiluca Scintillans* and nearby water.

Traffic density data were used in this study to determine oil slicks from ship origins. Here a global shipping traffic density dataset was used, which was created using hourly AIS positions received between January 2015 and February 2021 from the International Monetary Fund (IMF). The value of the traffic density data represents the total number of AIS positions that have been reported by ships in each grid cell (0.005° spatial resolution). The dataset was then down-sampled to 0.05° spatial resolution and divided by the total months in the above period to obtain the monthly average number of ships reported within the grid (0.05°, ~5.5 km at the equator).

After the detected slicks were determined not from oil platforms, a check of connected ships from the slick was executed. If a ship was directly associated with one end of the oil slick, the slick or nearby slicks would be classified as a vessel-originated slick. Otherwise, a simple traffic density threshold would be used to determine if the slicks originate from ships. The median traffic density not including the value of zero in the study area were chosen as the threshold. Here such a median value is 991, which means an average of 991 ships are reported to be within the extent of the grid in one month's time. Detected slicks with traffic densities surpass the threshold would be designated as vessel oil spills. If below the threshold, the detected slicks would be designated as from an unknown source.

3. Results

3.1. Delineated Oil Slicks

After inspecting and interpreting ~4800 Landsat 8 OLI images following the procedures described in Section 2.3, we identified 632 oil slicks in the NSCS from 2015 to 2019, among which 490 records were identified from ships, 57 from platforms, and 85 from unknown sources, accounting for 78%, 9%, and 13% of the total number of oil spills, respectively. Sources of oil slicks from ships mostly appeared as long strips (Figure 8), while some slicks showed irregular shapes. The shape of the slicks is usually determined by source types, discharged time, current and wind force. For example, the long narrow slick in Figure 8d was freshly released from a moving vessel (arrow pointed), and the earlier released part became wider because of the longer spreading time. The lower left of Figure 8d displays ship wakes from a moving vessel, which showed a typical V-shape with a dark region left behind. Figure 9 presents oil slicks determined from platform sources. As can be seen, all the slicks were directly connected to one or more of the platforms, usually with elongated shapes to one side of the platforms because of current and wind forces. Compared with ship-originated slicks, the shape of slicks from platform sources was often irregular (Figure 8 vs. Figure 9).

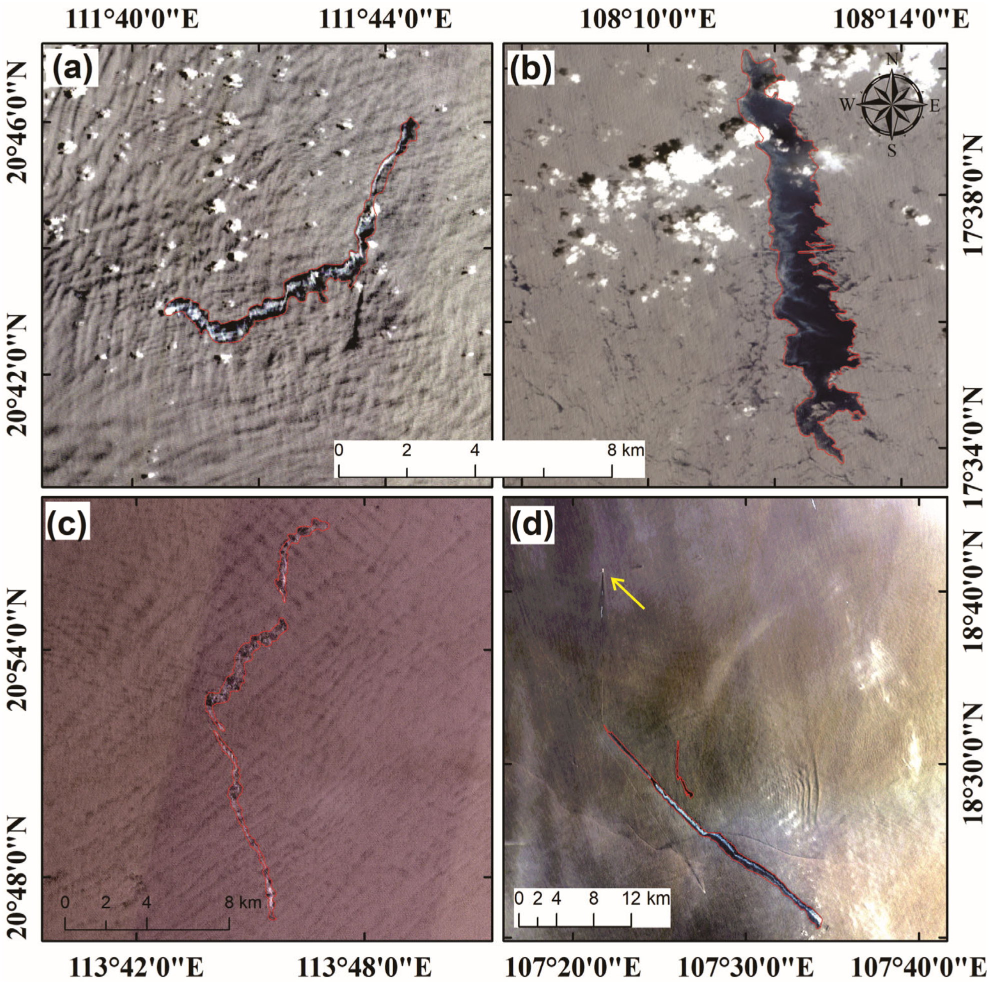

Figure 8. RGB imagery of oil slicks determined from ship sources in cases (**a**–**d**). Yellow arrow in panel d refers to the associated ship with the slicks.

3.2. Distribution of Oil Spills

The derived oil slick distribution map demonstrated large variability spatially and temporally (Figure 10). Year 2017 witnessed the highest oil-covered area (1208 km^2), 2018 the lowest (383 km^2), while there were fewer variations with other years (498–653 km^2). After combining all detected slicks, a cumulative oil pollution area of 3242 km^2 was determined in the NSCS from 2015 to 2019 (Figure 10). For individual slicks, the maximum area of detected slicks was 327 km^2 (35.5 after removing extremely large slicks). The average area of detected slicks was 4.8 km^2, with a median area of 1.7 km^2. The median area was significantly smaller than the mean because of extremely large spills pulling up the mean value. Several of the below regions showed a high incidence of oil spills: coastal areas from Shenzhen to Shantou, offshore regions from Wenchang to Yangjiang, the northeastern Beibu Gulf, and the middle of the south Beibu Gulf (Figure 10b). Overall, slicks were more frequently observed in the coastal region than in offshore waters. In reality, 50% of the oil spills were found within 33 km of the shoreline over the NSCS, and 90% of the oil spills were within 112 km of the shoreline. Particularly in the coastal Guangdong, the derived oil slicks were mostly in elongated shape and parallel to shorelines. In the Beibu Gulf, however, slicks were found to be distributed mostly offshore, where detected slicks tended to be in irregular shapes.

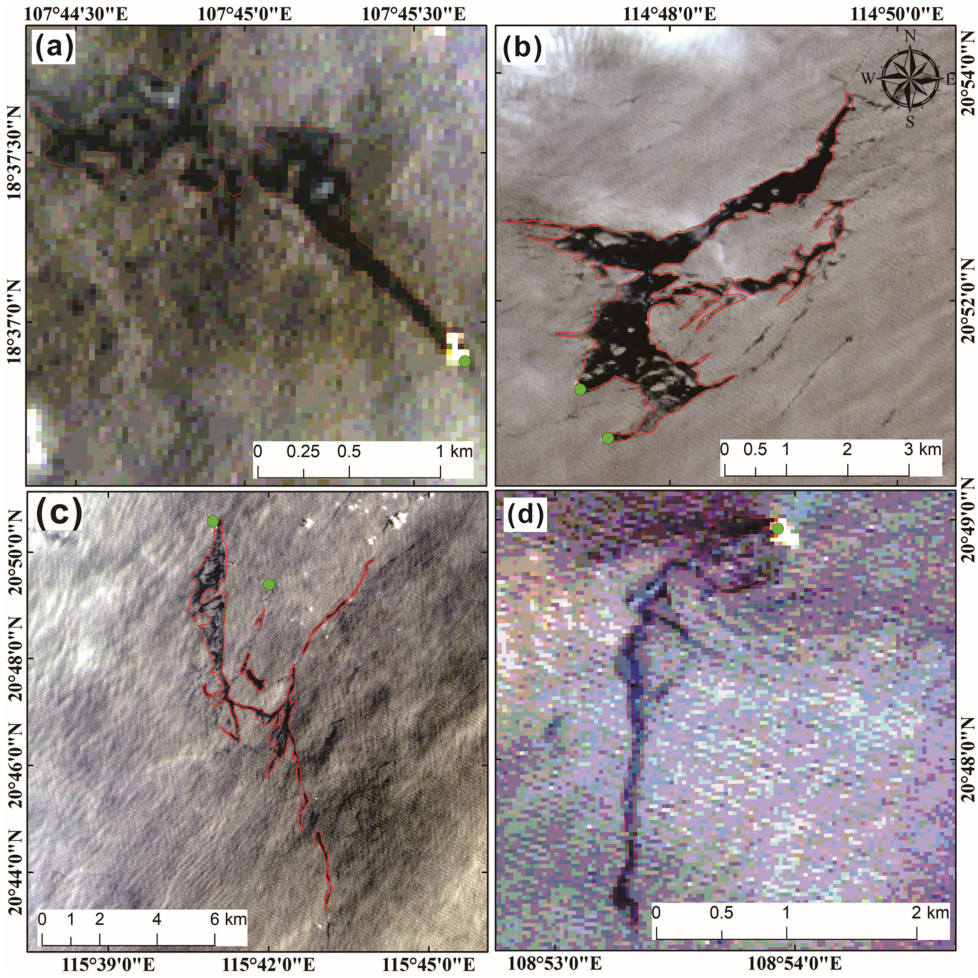

Figure 9. RGB imagery of oil slicks determined from platform sources in cases (**a**–**d**). The green dots denote oil platform locations.

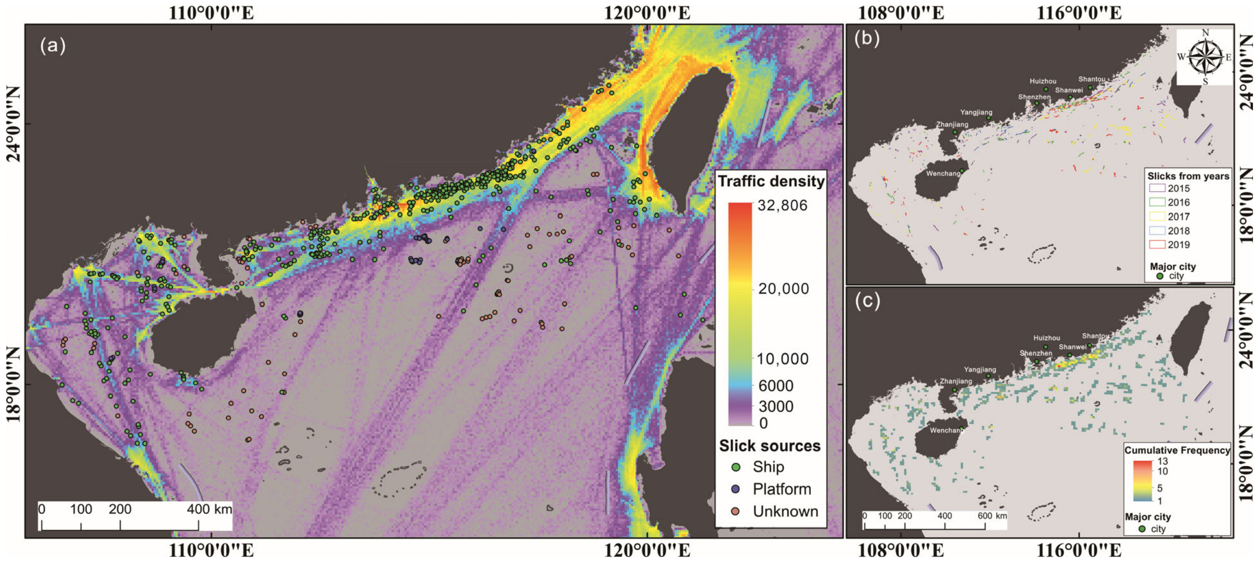

Figure 10. (**a**) Traffic density and the determined slick origins in the study area; (**b**) distribution of oil spills in the NSCS; (**c**) oil slick cumulative distribution (grid: 10 × 10 km^2).

The extracted oil slicks were further binned into 10 × 10 km^2 grids (Figure 10c), where the value of the grid denoted the number of times the detected slicks covered this region during 2015–2019. Oil slicks were most frequently observed south of Huizhou city, where a total of 13 oil spills were detected. The coastal area from Shenzhen to Shantou represented a high incidence of oil spill regions in the NSCS (Figure 10c). Eight oil slicks were detected in the offshore area east of Hainan Island. However, the above hot spot was within one grid, where surrounding waters scarcely detected oil presence.

We further select two sub-regions to present detailed information on oil slick distribution spatially and temporally: the Guangdong–Hong Kong–Macao Greater Bay Area (GBA, Figure 11a) and the northeastern Beibu Gulf (Figure 11b). GBA includes three of the world's busiest ports (Guangzhou, HongKong, and Shenzhen) and is an important marine traffic hub in Southeast Asia. The Beibu Gulf Basin is a major oil and gas reserve located in the northeastern Beibu Gulf as stated in Section 2. Oil slicks in GBA were most frequently observed off the coast in the east side of the Pearl River Estuary (PRE), most of which were from ships. Oil spill cases in this region ranged from 30 to 50 yearly in this region, with average oil spills of ~40 cases each year (Table 2). The years 2016 and 2019 witnessed the largest slicks that exceeded 30 km^2, with the rest years at ~23 km^2. The years 2015, 2016, and 2019 witnessed the largest total polluted area (~160 km^2). The median slick area was ~1.6 km^2 each year. Seasonally, there was a clear pattern that spills were more frequently observed in spring and summer than in fall and winter in the GBA (Table 2).

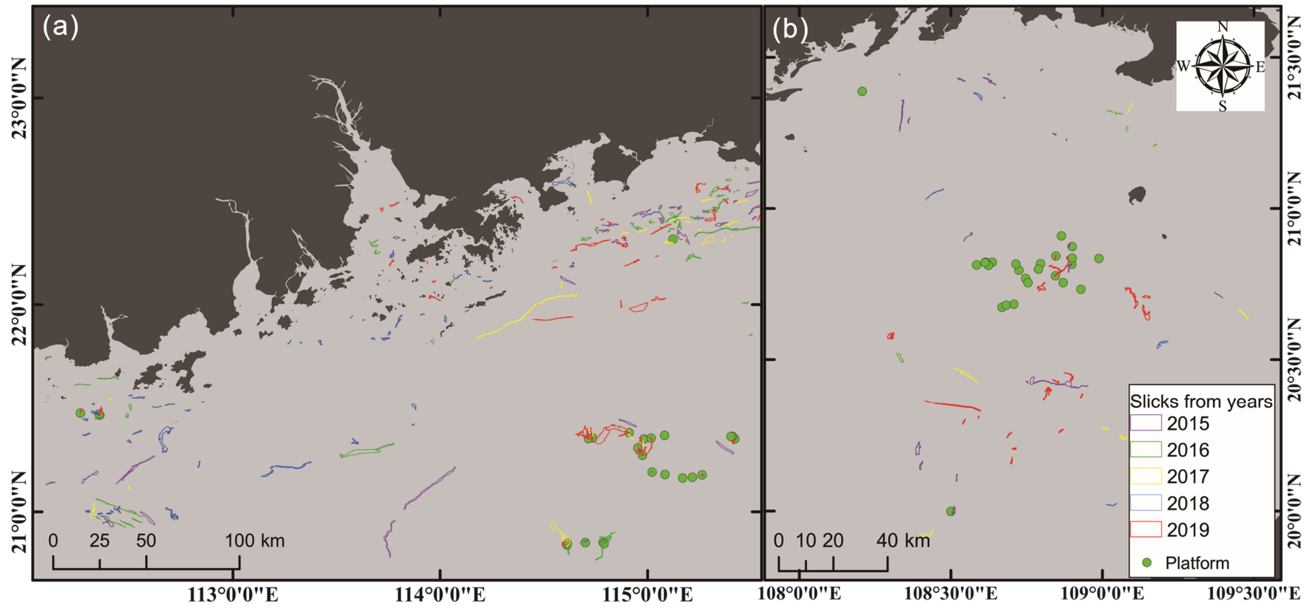

Figure 11. Distribution of oil slicks in: (**a**) the Guangdong–Hong Kong–Macao Greater Bay Area; and (**b**) northeastern Beibu Gulf. Black points denote oil platforms location.

Table 2. Statistical data for delineated oil slicks in the Guangdong–Hong Kong–Macao Greater Bay Area.

Year	Spring (Times)	Summer (Times)	Fall (Times)	Winter (Times)	Total (Times)	Maximum Area (km^2)	Minimum Area (km^2)	Average Area (km^2)	Median Area (km^2)	Total Area (km^2)
2015	27	8	7	0	42	21.1	0.24	3.7	2.0	154.4
2016	17	21	6	0	44	35.5	0.21	3.8	2.0	165.0
2017	3	22	0	2	27	22.7	0.30	3.5	1.1	94.3
2018	25	21	0	0	46	26.9	0.21	2.7	1.0	124.8
2019	22	0	13	4	39	33.8	0.21	4.4	2.1	170.0

In the northeastern Beibu Gulf, a similar seasonal trend can be observed in 2015, 2016, and 2018 (Table 3). Only occasional oil spills (seven cases) were detected to originate from platforms in this region. Other than that, most of the detected slicks (39 cases) were from ships. The overall percentage of oil spills from platforms was only 14% in the number of slicks and 7% in the area, respectively. The same percentage became 15% in number of slicks and 21% in area in the GBA. From 2016 to 2018, both the number of oil slicks (~6 vs. ~15) and total oil polluted area (<10 vs. >20 km^2) were relatively small compared to those of slicks detected in 2015 and 2019 in this region. The average yearly slick area was almost one magnitude smaller (~15 vs. 140 km^2) than areas in the GBA, partly because of the smaller size of this sub-region.

Table 3. Statistical data for delineated oil slicks in the Beibu Gulf.

Year	Spring (Times)	Summer (Times)	Fall (Times)	Winter (Times)	Total (Times)	Maximum Area (km^2)	Minimum Area (km^2)	Average Area (km^2)	Median Area (km^2)	Total Area (km^2)
2015	9	0	0	5	14	9.1	0.25	1.6	0.8	23.3
2016	6	0	0	1	7	2.9	0.36	1.1	0.5	7.8
2017	0	3	0	3	6	3.6	0.34	1.5	1.2	9.3
2018	2	4	0	0	6	2.4	0.24	1.0	0.6	6.1
2019	6	1	10	0	17	4.7	0.22	1.4	0.6	24.0

3.3. Cross-Check

Because of the ocean surface dynamics and oil weathering processes, it is rather difficult to validate remote sensing interpretation with field measurements [30,40]. In this study, we use imagery from high-resolution PlanetScope to cross-check the OLI detections. A total of 26 same-day PlanetScope/OLI matching pairs were found from March to October 2018. All of the matched same-day PlanetScope images detected oil slicks in the same region. The corresponding PlanetScope images were then delineated for area comparison. The comparison of oil slick delineated results from the two sensors are listed in Table 4. Here the Unbiased Mean Relative Error (UMRE) was used to estimate the relative detection area error between the two sensors (Equation (1)), with UMRE calculated to be 17% [25]. Not all of the slick pairs were compared for area because of incomplete spill size by cloud cover or by image swath limit. Figure 12 shows oil slicks by the OLI/PlanetScope image pairs. Because both OLI and PlanetScope are optical sensors, their imaging time of the same-day is usually within a few hours or even a few minutes. The oil slick in OLI imagery was similar to the oil slick in PlanetScope in shape and area (Figure 12a–c, UMRE < 47%), with the largest oil area difference in Figure 12d (UMRE = 133%).

$$\text{UMRE} = \frac{1}{n}\sum_{i=1}^{n}\left|\frac{x_i - y_i}{0.5x_i + 0.5y_i}\right| \quad (1)$$

where x_i, y_i are the area of the delineated oil slicks from the two images, respectively.

Table 4. Comparison of oil slick delineated results from the two sensors.

Slick	Imaging Time	Location	Time Difference (Min)	Slick Area from OLI (m^2)	Slick Area from PlanetScope (m^2)	UMRE
1	14 October 2018	20°42′N, 109°24′E	19	1,388,000	1,390,000	0.002
2	20 September 2018	18°54′N, 107°18′E	13	11,160,000	11,590,000	0.038
3	20 September 2018	20°42′N, 109°24′E	22	25,400,000	26,940,000	0.059
4	21 August 2018	20°00′N, 109°00′E	3	287,600	211,100	0.307
5	7 August 2018	18°54′N, 112°42′E	18	6,473,000	9,454,000	0.374
6	7 August 2018	21°30′N, 112°42′E	3	1,286,000	1,224,000	0.049
7	2 August 2018	23°18′N, 117°24′E	13	4,359,000	2,865,000	0.414
8	1 July 2018	24°42′N, 119°00′E	24	1,248,000	784,800	0.456
9	18 June 2018	17°00′N, 108°30′E	11	7,358,000	6,761,000	0.085
10	9 June 2018	21°00′N, 108°30′E	4	825,000	723,900	0.130
11	23 May 2018	22°36′N, 119°48′E	24	3,826,000	4,458,000	0.153
12	23 May 2018	22°36′N, 119°48′E	24	1,392,000	1,389,000	0.003

Table 4. *Cont.*

Slick	Imaging Time	Location	Time Difference (Min)	Slick Area from OLI (m^2)	Slick Area from PlanetScope (m^2)	UMRE
13	21 May 2018	22°36′N, 116°36′E	22	1,276,000	1,251,000	0.020
14	21 May 2018	22°24′N, 116°30′E	22	3,438,000	3,887,000	0.123
15	19 May 2018	21°18′N, 112°36′E	21	24,150,000	26,220,000	0.082
16	17 May 2018	20°42′N, 109°24′E	10	278,300	355,100	0.243
17	14 May 2018	23°24′N, 118°18′E	23	19,640,000	15,270,000	0.250
18	1 May 2018	18°12′N, 108°30′E	20	706,820	628,937	0.117
19	1 April 2018	21°54′N, 114°00′E	27	1,317,000	2,061,000	0.441
20	29 March 2018	20°42′N, 109°24′E	26	7,935,000	9,129,000	0.140

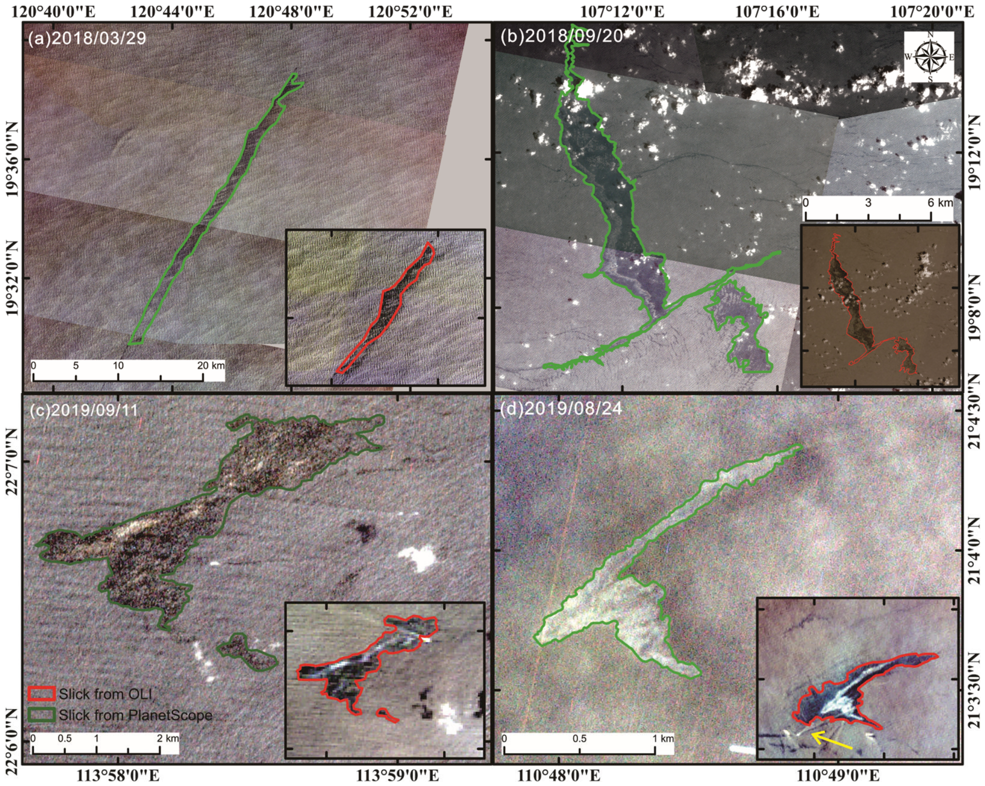

Figure 12. Same day image pairs from PlanetScope and OLI (insets), with a time difference of: (**a**) 26 min; (**b**) 13 min; (**c**) 13 min; and (**d**) 18 min, respectively. The yellow arrow from the panel d inset is pointed to moving ship directly connected to the slicks, which was determined to be not released from the pointed ship.

4. Discussion

4.1. Slick Distribution from Different Sources

Origins of the delineated slicks are shown in Figure 10a. Spatial cluster analysis was performed using Getis-Ord Gi * in GeoDa (Version:1.18, The University of Chicago, Chicago, U.S.) to analyze the clustering effect of oil spill distribution from different sources and areas [41,42]. Figure 13a shows regions of significant slick spatial clustering from offshore platforms (red color) and ships (blue) ($p < 0.05$), which indicated oil slick clusters from offshore platforms in the southeast of the PRE, east the Hainan Island, the middle of the south Beibu Gulf, and oil slick clusters from ship sources east of the PRE along the Guangdong coast, northeast of Dongsha Island, east of Zhanjiang city, and in the middle of the south Beibu Gulf. Figure 13b shows results of spatial clustering from slick areas. Significant large slicks were mainly distributed southwest and northeast of Dongsha Island, while significant small slicks were distributed slightly east of the PRE, south of Yangjiang, and scattered in the northeastern Beibu Gulf. As can be seen, smaller areas of slicks were mainly clustered along the coast (half of the slicks were within 54 km of the shoreline), while the significant large slicks were clustered in offshore waters (all the slicks were >147 km from the shoreline). Moreover, none of the significant large slick clusters was associated with oil platforms, indicating that platform spills tended to have smaller oil spill sizes in the study area. The smaller size of platform slicks can also be summarized from slick area histograms, which clearly presented larger area distribution from ship or unknown sources than from platform sources (Figure 14a).

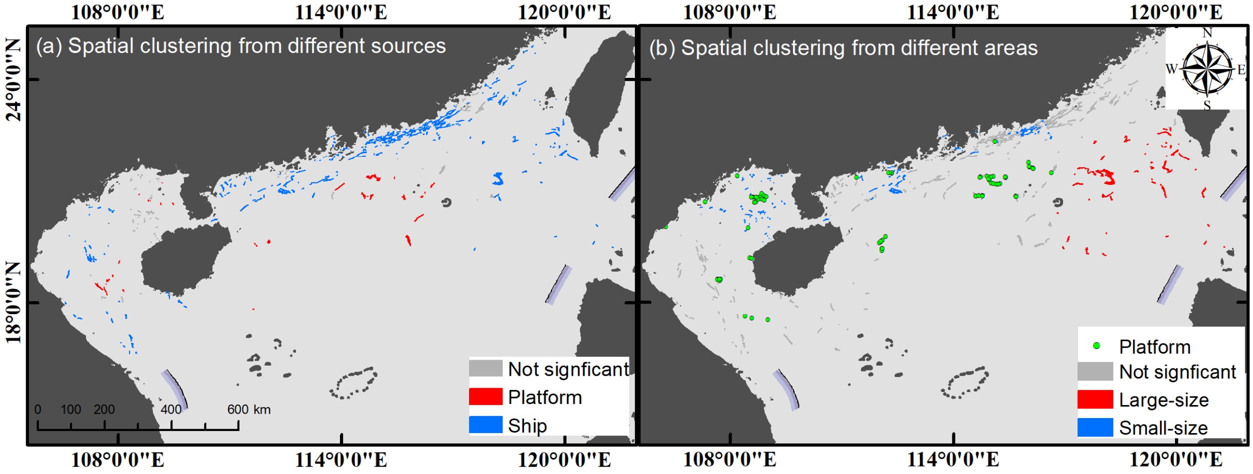

Figure 13. The spatial cluster of oil slicks: (**a**) from different sources: and (**b**) from different areas determined by the Gi * method.

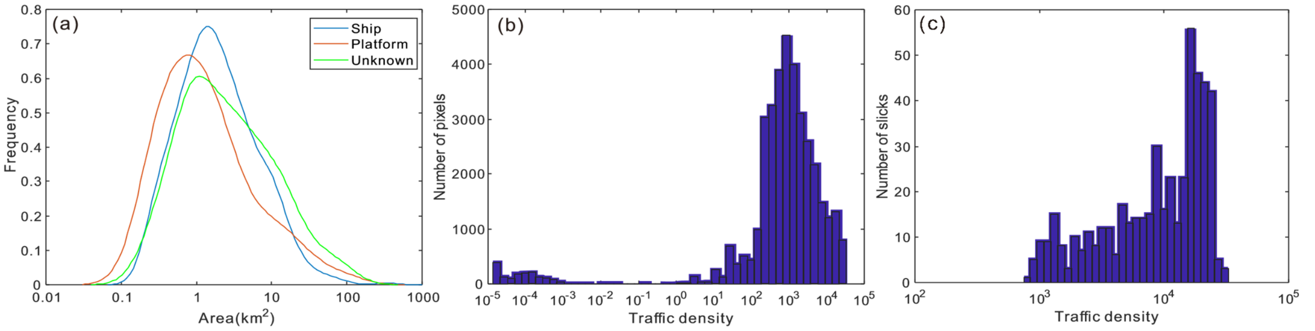

Figure 14. (**a**) The frequency distribution of slick areas from different sources; the frequency distribution histogram of traffic density: (**b**) in the study area; and (**c**) in the slick regions of ship origins.

The cumulative oil distribution map demonstrated wide slick cover over the joint fishing zone between China and Vietnam in the Beibu Gulf (Figure 10c, [43]). Moreover, a noticeable disparity of oil distributions can be found between the east and west side of the PRE (Figure 10b), and a significant oil slick cluster from ship sources is found in the east side of the PRE mouth. Such disparity coincides with the several major maritime traffic belts in this region, which travels from east of Hainan Island to the GBA and then to the east and north along the Guangdong coast, as also demonstrated in the traffic density map (Figure 10a) [44,45]. Similar results have been found from statistical analysis of crude oil tanker accidents, which reveal a positive correlation between traffic density and crude oil tanker accidents [46].

4.2. Uncertainties

Same-day image pairs were used to cross-check the OLI result. The OLI/Sentinel-1 SAR image pairs were searched, with sensing time differences ranging from 5 to 19 h.

Part of the slicks was detected in both SAR and OLI, with small variations in shape or area (Figure S1). However, some of the OLI-determined slicks were not detected by the same-day SAR imagery, or the shapes of the SAR-detected slick were quite different from OLI. A hindcast model from natural slicks (with slick lengths ranging from 1 to 50 km) in the GoM suggests a life span of 6.4 (±5.7) h of the detected slicks [47]. Slicks from natural seeps in the Lower Congo Basin are found to have residence time between 1 and 7 h, with an average of 3 h 15 min [48]. With the above time difference between SAR and OLI imaging, the surface slick or part of the surface slicks could disappear because of the oil weathering processes. Therefore, only results from the optical PlanetScope with sensing time a few minutes apart from OLI were compared for areal statistical analysis (Table 4). Figure 12d shows oil slicks detected by OLI and PlanetScope at a time difference of 2 min, but with an area difference of 133%. Clearly, little slick variation was expected between such a small time difference. When we looked into the two images, we found that the bright part of the two images had similar shapes, with an area difference of 20%. The dark part of the slicks in OLI was not effectively detected by PlanetScope, which could be because of the weak sun glint intensity in the PlanetScope image or because of the relatively low signal-to-noise ratio of the PlanetScope image. The estimated relative error of the OLI-determined area from PlanetScope was 17%. Such a difference represents uncertainties from manual delineation, scattered cloud cover (scattered cloud moved during the time difference), and the oil detection abilities of different sensors.

Thick oil can be detected through the reflectance response in the visible-NIR-SWIR range, while thin oil slicks are detectable because of the sun glint in optical imagery [38,39]. In fact, both of the mechanisms are used in optical imagery to detect the slick-caused spatial contrast and to rule out oil look-alikes spectrally [30,40]. However, in the absence of sun glint ($L_{GN} < 10^{-6}$ sr^{-1} for MODIS for example, because of unfavorable solar and view angels, and wind conditions), thin oil is undetectable in optical imagery [40]. Such sun glint strength is relatively higher in April to September than during the rest of the year in the mid-latitude Northern Hemisphere [25,40]. In reality, 99.5% of the detected slicks were within optimal wind conditions for slick detection under sun glint (1–8 m/s, Figure S2) [31]. Moreover, optical imagery suffers from cloud cover, which is useless if the slick is fully covered by cloud. Therefore, the derived slick distribution by the optical OLI imagery in this study represented a subset of all slicks on the ocean surface during the time period.

Other than the traffic density data, we used a rule of ship-connection to justify slick origin from ships, which was not always true. As shown in the Figure 12d inset, there was a moving ship connected to the slick, but the slick was most possibly not released from the ship considering slick width (>2 km) (time required for spreading) as the ship was still moving at the scene time. Nevertheless, the slick was still identified to be from ships because of the traffic density in this region (11,800 > threshold 991), and it might have been released by another ship outside the scene at the imaging time.

5. Conclusions

In this study, the medium resolution optical Landsat-8 OLI imagery was used to delineate oil slicks in the NSCS. The source of the detected oil slicks was determined from an offshore oil and gas platform database and the traffic density data in the study area. A total of 632 oil slicks were identified, with cumulative oil pollution of 3242 km^2 in the NSCS from 2015 to 2019. Of all the slicks detected, 57 were determined to be from platform sources, 490 from ship sources, and the rest from unknown sources. The average area of detected slicks was 4.8 km^2, with half of the slick area <1.7 km^2. Our results show that 90% of the oil spills were found within 112 km of the shoreline, and half of the slicks were within 33 km from shorelines. Spatial clustering analysis indicated that slicks from ship sources were significantly clustered east of the PRE along the Guangdong coast, northeast of the Dongsha Island, east of Zhanjiang city, and in the middle of the south Beibu Gulf, and slicks from platform sources were significantly clustered southeast of the PRE, east Hainan Island, and in the middle of the south Beibu Gulf. Moreover, slicks from ship or unknown sources tended to have larger areas than slicks from platforms in the study area. Results from this study demonstrate the capability of medium-resolution OLI imagery in detecting and monitoring oil spills regionally, and the derived oil distribution map in the NSCS would hopefully provide useful information for future environmental assessments of the chronic oil spills.

Supplementary Materials: The following supporting information can be downloaded at: https://www.mdpi.com/article/10.3390/rs14163966/s1, Figure S1: Comparison of same-day image pairs from Sentinel-1 SAR and Landsat-8 OLI; Figure S2: Histogram of wind speed for all the delineated slicks.

Author Contributions: Conceptualization, S.S.; methodology, X.H., L.C. and S.S.; writing—original draft preparation, X.H. and L.C.; writing—review and editing, X.H., L.C., S.S., Z.S., Y.C., Q.M. and Z.C.; funding acquisition, S.S. and L.C. All authors have read and agreed to the published version of the manuscript.

Funding: This research was funded by the Guangdong Basic and Applied Basic Research Foundation, grant number 2020A1515110957, the National Natural Science Foundation of China, grant number 42106173, the Sun Yat-sen University Undergraduate Innovation Program, grant number 20201430, and the Dragon 5 Cooperation, grant number 59193.

Data Availability Statement: Landsat-8 data are openly accessible from https://earthexplorer.usgs.gov/, accessed on 11 July 2022, global shipping traffic density data are openly accessible from https://datacatalog.worldbank.org/search/dataset/0037580/Global-Shipping, accessed on 11 July 2022.

Acknowledgments: The authors would like to thank USGS for providing Landsat data, Planet Labs for providing PlanetScope data, and IMF for providing the shipping traffic density data.

Conflicts of Interest: The authors declare no conflict of interest.

References

1. DOINews. *DOINews: Scientific Teams Refine Estimates of Oil Flow from BP's Well Prior to Capping*; U.S. Department of the Interior: Washington, DC, USA, 2010; Volume 2022.
2. Sun, S.; Lu, Y.; Liu, Y.; Wang, M.; Hu, C. Tracking an oil tanker collision and spilled oils in the East China Sea using multisensor day and night satellite imagery. *Geophys. Res. Lett.* **2018**, *45*, 3212–3220. [CrossRef]
3. Hebbar, A.A.; Dharmasiri, I.G. Management of marine oil spills: A case study of the Wakashio oil spill in Mauritius using a lens-actor-focus conceptual framework. *Ocean Coast. Manag.* **2022**, *221*, 106103. [CrossRef]
4. International Tanker Owners Pollution Federation (ITOPF). Oil Tanker Spill Statistics 2021. Available online: https://www.itopf.org/knowledge-resources/data-statistics/statistics (accessed on 11 July 2022).
5. National Research Council (US). *Oil in the Sea III: Inputs, Fates, and Effects*; National Academies Press (US): Washington, DC, USA, 2003.
6. Fingas, M. *The Basic of Oil Spill Clean Up*, 3rd ed.; CRC Press: Boca Raton, FL, USA, 2012.
7. Dong, Y.; Liu, Y.; Hu, C.; MacDonald, I.R.; Lu, Y. Chronic oiling in global oceans. *Science* **2022**, *376*, 1300–1304. [CrossRef] [PubMed]
8. Laffon, B.; Pásaro, E.; Valdiglesias, V. Effects of exposure to oil spills on human health: Updated review. *J. Toxicol. Environ. Health Part B Crit. Rev.* **2016**, *19*, 105–128. [CrossRef] [PubMed]
9. Keramea, P.; Spanoudaki, K.; Zodiatis, G.; Gikas, G.; Sylaios, G. Oil spill modeling: A critical review on current trends, perspectives, and challenges. *J. Mar. Sci. Eng.* **2021**, *9*, 181. [CrossRef]
10. U.S. Environmental Protection Agency (EPA). Oil Discharge Reporting Requirements. Available online: https://www.epa.gov/sites/default/files/2014-06/documents/spccfactsheetspillreportingdec06-1.pdf (accessed on 11 July 2022).
11. Daneshgar Asl, S.; Amos, J.; Woods, P.; Garcia-Pineda, O.; MacDonald, I.R. Chronic, anthropogenic hydrocarbon discharges in the Gulf of Mexico. *Deep Sea Res. Part II Top. Stud. Oceanogr.* **2016**, *129*, 187–195. [CrossRef]
12. Chen, Q.; Hu, S. Study on offshore oil spill accidents in China. *Mar. Dev. Manag.* **2020**, *37*, 49–53.
13. Gong, Y.; Zhao, P.; Lan, D.; Zhu, R.; Yan, X.U.; Bao, C.; Chunyan, Y.U. Characteristics and trend analysis of marine oil spill accidents in China. *Ocean Dev. Manag.* **2018**, *35*, 42–45.
14. Brekke, C.; Solberg, A. Oil spill detection by satellite remote sensing. *Remote Sens. Environ.* **2005**, *95*, 1–13. [CrossRef]
15. Fingas, M.; Brown, C. Review of oil spill remote sensing. *Mar. Pollut. Bull.* **2014**, *83*, 9–23. [CrossRef]
16. Leifer, I.; Lehr, W.J.; Simecek-Beatty, D.; Bradley, E.; Clark, R.; Dennison, P.; Hu, Y.; Matheson, S.; Jones, C.E.; Holt, B.; et al. State of the art satellite and airborne marine oil spill remote sensing: Application to the BP Deepwater Horizon oil spill. *Remote Sens. Environ.* **2012**, *124*, 185–209. [CrossRef]

17. Kokaly, R.F.; Couvillion, B.R.; Holloway, J.; Roberts, D.A.; Ustin, S.L.; Peterson, S.H.; Khanna, S.; Piazza, S.C. Spectroscopic remote sensing of the distribution and persistence of oil from the Deepwater Horizon spill in Barataria Bay marshes. *Remote Sens. Environ.* **2013**, *129*, 210–230. [CrossRef]
18. Lu, Y.; Zhan, W.; Hu, C. Detecting and quantifying oil slick thickness by thermal remote sensing: A ground-based experiment. *Remote Sens. Environ.* **2016**, *181*, 207–217. [CrossRef]
19. Garcia-Pineda, O.; MacDonald, I.; Hu, C.; Svejkovsky, J.; Hess, M.; Dukhovskoy, D.; Morey, S.L. Detection of floating oil anomalies from the Deepwater Horizon oil spill with synthetic aperture radar. *Oceanography* **2013**, *26*, 124–137. [CrossRef]
20. Mohr, V.; Gade, M. Marine oil pollution in an area of high economic use: Statistical analyses of SAR data from the Western Java Sea. *Remote Sens.* **2022**, *14*, 880. [CrossRef]
21. Trinadha Rao, V.; Suneel, V.; Raajvanshi, I.; Alex, M.J.; Thomas, A.P. Year-to-year variability of oil pollution along the Eastern Arabian Sea: The impact of COVID-19 imposed lock-downs. *Mar. Pollut. Bull.* **2022**, *175*, 113356. [CrossRef]
22. Garcia-Pineda, O.; MacDonald, I.R.; Li, X.; Jackson, C.R.; Pichel, W.G. Oil spill mapping and measurement in the Gulf of Mexico with Textural Classifier Neural Network Algorithm (TCNNA). *IEEE J. Sel. Top. Appl. Earth Obs. Remote Sens.* **2013**, *6*, 2517–2525. [CrossRef]
23. Hu, C.; Weisberg, R.H.; Liu, Y.; Zheng, L.; Daly, K.L.; English, D.C.; Zhao, J.; Vargo, G.A. Did the northeastern Gulf of Mexico become greener after the Deepwater Horizon oil spill? *Geophys. Res. Lett.* **2011**, *38*, L09601. [CrossRef]
24. Hu, C.; Li, X.; Pichel, W.G.; Muller-Karger, F.E. Detection of natural oil slicks in the NW Gulf of Mexico using MODIS imagery. *Geophys. Res. Lett.* **2009**, *36*, L1604. [CrossRef]
25. Sun, S.; Hu, C.; Garcia-Pineda, O.; Kourafalou, V.; Le Hénaff, M.; Androulidakis, Y. Remote sensing assessment of oil spills near a damaged platform in the Gulf of Mexico. *Mar. Pollut. Bull.* **2018**, *136*, 141–151. [CrossRef]
26. Chen, T. Study on rapid prediction of oil spill drift in the east of the South China Sea. *China Pet. Chem. Stand. Qual.* **2020**, *5*, 168–172.
27. Chang, P.; Yang, Q. Necessity and feasibility of establishing a particularly sensitive sea area system in the South China Sea. *Water Transp. Manag.* **2018**, *15*, 6–8.
28. Vanhellemont, Q. Adaptation of the dark spectrum fitting atmospheric correction for aquatic applications of the Landsat and Sentinel-2 archives. *Remote Sens. Environ.* **2019**, *225*, 175–192. [CrossRef]
29. Planet Team. Planet Team. Planet Application Program Interface. In *Space for Life on Earth*; Planet Team: San Francisco, CA, USA, 2017. Available online: https://api.planet.com (accessed on 11 July 2022).
30. Sun, S.; Hu, C. The challenges of interpreting oil–water spatial and spectral contrasts for the estimation of oil thickness: Examples from satellite and airborne measurements of the Deepwater Horizon oil spill. *IEEE Trans. Geosci. Remote* **2019**, *57*, 2643–2658. [CrossRef]
31. Sun, S.; Hu, C. Sun glint requirement for the remote detection of surface oil films. *Geophys. Res. Lett.* **2016**, *43*, 309–316. [CrossRef]
32. Sun, S.; Hu, C.; Feng, L.; Swayze, G.A.; Holmes, J.; Graettinger, G.; Macdonald, I.; Garcia, O.; Leifer, I. Oil slick morphology derived from AVIRIS measurements of the Deepwater Horizon oil spill: Implications for spatial resolution requirements of remote sensors. *Mar. Pollut. Bull.* **2016**, *103*, 276–285. [CrossRef]
33. Liu, Y.; Zhao, J.; Qin, Y. A novel technique for ship wake detection from optical images. *Remote Sens. Environ.* **2021**, *258*, 112375. [CrossRef]
34. Liu, Y.; Deng, R. Ship wakes in optical images. *J. Atmos. Ocean. Technol.* **2018**, *35*, 1633–1648. [CrossRef]
35. Hu, C.; Feng, L.; Hardy, R.F.; Hochberg, E.J. Spectral and spatial requirements of remote measurements of pelagic Sargassum macroalgae. *Remote Sens. Environ.* **2015**, *167*, 229–246. [CrossRef]
36. Bin, Y.I.; Chen, K.; Zhou, J.; Yihua, L.U. Characteristics of red tide in coastal region of South China from 2009 to 2016. *Trans. Oceanol. Limnol.* **2018**, *2*, 23–31.
37. Tian, Y.; Li, T.; Hu, S.; Xie, X.; Liu, S. Temporal and spatial characteristics of harmful algal blooms in Guangdong coastal area. *Mar. Environ. Sci.* **2020**, *39*, 1–8.
38. Qi, L.; Tsai, S.F.; Chen, Y.; Le, C.; Hu, C. In search of red Noctiluca scintillans blooms in the East China Sea. *Geophys. Res. Lett.* **2019**, *46*, 5997–6004. [CrossRef]
39. Liu, Y.; Hu, C.; Sun, C.; Zhan, W.; Sun, S.; Xu, B.; Dong, Y. Assessment of offshore oil/gas platform status in the northern Gulf of Mexico using multi-source satellite time-series images. *Remote Sens. Environ.* **2018**, *208*, 63–81. [CrossRef]
40. Hu, C.; Lu, Y.; Sun, S.; Liu, Y. Optical remote sensing of oil spills in the ocean: What is really possible? *J. Remote Sens.* **2021**, *2021*, 9141902. [CrossRef]
41. Getis, A.; Ord, J.K. The Analysis of Spatial Association by Use of Distance Statistics. *Geogr. Anal.* **1992**, *24*, 189–206. [CrossRef]
42. Mitchell, A. *The Esri Guide to GIS Analysis Volume 2: Spatial Measurements & Statistics*, 2nd ed.; Esri Press: Redlands, CA, USA, 2021.
43. Pan, P.; Luo, J.C.; Yi-Yun, H.U. Review of fishery cooperative agreement in Beibu Gulf between the People's Republic of China and the Socialist Republic of Vietnam. *Chin. Fish. Econ.* **2016**, *34*, 22–26.
44. Wu, L.; Xu, Y.; Wang, Q.; Wang, F.; Xu, Z. Mapping global shipping density from AIS data. *J. Navig.* **2017**, *70*, 67–81. [CrossRef]
45. Mei, Q.; Lin, W.U.; Peng, P. Typical spatial distribution of merchant vessels and trade flow in South China Sea. *J. Geo-Inf. Sci.* **2018**, *20*, 632–639.
46. Wang, J.; Zhou, Y.; Zhuang, L.; Shi, L.; Zhang, S. Study on the critical factors and hot spots of crude oil tanker accidents. *Ocean Coast. Manag.* **2022**, *217*, 106010. [CrossRef]

47. Daneshgar Asl, S.; Dukhovskoy, D.S.; Bourassa, M.; Macdonald, I.R. Hindcast modeling of oil slick persistence from natural seeps. *Remote Sens. Environ.* **2017**, *189*, 96–107. [CrossRef]
48. Jatiault, R.; Dhont, D.; Loncke, L.; Dubucq, D. Monitoring of natural oil seepage in the Lower Congo Basin using SAR observations. *Remote Sens. Environ.* **2017**, *191*, 258–272. [CrossRef]